Energy & Environmental Science

ARTICLE

Sequential catalysis controls selectivity in electrochemical CO_2 reduction on Cu†

Received 00th January 20xx,
Accepted 00th January 20xx

DOI: 10.1039/x0xx00000x

www.rsc.org/

Yanwei Lum[ab] and Joel W Ager*[ab]

Electrochemical reduction of CO_2 in aqueous media is a strategy for sustainable production of fuels and commodity chemicals. Cu is the only catalyst which converts CO_2 to significant quantities of hydrocarbons and oxygenates. Here we demonstrate that oxygenate products can be favored over hydrocarbons by positioning a local source of CO generated by a CO producing catalyst (Au or Ag) in close proximity to a Cu catalyst. Use of a bimetallic device comprising interdigitated and independently controllable lines of Au and Cu allows the local CO concentration to be modulated. Notably, diffusional simulations show that the saturation concentration of CO can be exceeded locally. Actuating both the Au and Cu lines increases the oxygenate to ethylene ratio compared to actuating Cu only. Increasing the relative area of CO-producing Au relative to Cu also increases this ratio. These insights are translated into a second bimetallic system comprising Cu dots/lines patterned directly onto a Ag substrate, allowing for the distance between Cu and the CO generating metal to be precisely controlled. Controlling the relative areas of Ag and Cu allows for tuning of the oxygenate to ethylene ratio from 0.59 to 2.39 and an increase in oxygenate faradaic efficiency from 21.4% to 41.4%, while maintaining the selectivity to C_2/C_3 products in the 50-65% range. We attribute this change in selectivity to be due to an increased *CO coverage on Cu. By utilizing diffusional transport of CO to the Cu, a sequential catalysis pathway is created which allows for the control of oxygenate selectivity in aqueous CO_2 reduction.

Broader Context

Electrochemical reduction of CO_2 to form fuels and/or chemical feedstocks represents a potential path towards reducing CO_2 emissions and combatting global climate change. However, despite decades of research, electrocatalysts with the requisite activity and selectivity to commercially develop this process have not been discovered. Inspired by the multi-step enzymatic pathways found in the Calvin cycle, a two-step sequential electrocatalysis pathway is demonstrated which uses CO as an intermediate species. The higher areal density of active sites on metals as compared to enzymes allow diffusional transport of intermediates over micron length scales and thus allows bimetallic sequential catalysis devices to be fabricated with standard photolithographic techniques. The sequential catalysis pathway dramatically increases the yield of oxygenated products when Cu is used as the second catalyst in the sequence. This approach represents a new paradigm in the design of selective catalysts for electrochemical CO_2 reduction. The bimetallic design is essential modular, allowing for individual components to be optimized before integration, potentially allowing for entirely new libraries of catalysts to be explored.

Introduction

Electrochemical reduction of CO_2 (EC CO_2R) to chemical fuels and feedstocks via the use of renewable electrical energy is a potential way to mitigate rising atmospheric CO_2 emissions.[1–4] There has therefore been considerable interest in developing efficient and selective electrocatalysts to facilitate this chemical conversion process.[5–13] Of the electrocatalysts investigated to date for CO_2R in aqueous solution, Cu remains the only catalyst with significant faradaic yields of C_{2+} hydrocarbons and oxygenates.[14–16] However, selectivity towards a specific product such as ethylene or ethanol is not yet high enough to be relevant for practical implementation.[1,15] Therefore, enhancing the selectivity towards products with 2 or more carbons (C_2/C_3), which tend to be more valuable as feedstock and fuels[17] is an attractive technological target.[11,12]

Reduction of CO on Cu produces a similar product distribution as CO_2R,[18] albeit with a much lower current density due to the lower solubility of CO in water (~1 mM vs. ~33 mM for CO_2 at 1 atm and 25 °C).[19–21] A number of first principles

[a] Joint Center for Artificial Photosynthesis and Materials Science Division, Lawrence Berkeley National Laboratory, California 94720, United States
[b] Department of Materials Science and Engineering, University of California, Berkeley, California 94720, United States

†Electronic Supplementary Information (ESI) available: simulation details, fabrication and images of interdigitated devices, fabrication and images of line/dot devices, supplemental electrocatalysis data, control experiments and simulations. See DOI: 10.1039/x0xx00000x

calculations have shown that all known products of CO_2R on Cu, with the exception of formate, have CO as the primary intermediate.[22–29] It is thus reasonable to expect that changes in CO activity at the surface of a Cu electrode could affect the product distribution. In fact, very recently it has been predicted that "CO dimerization [could be accelerated]… by increasing the local concentration of CO by conjoining Cu with another element such as Ag or Au that can produce CO from CO_2," although a method for creating these conditions was not specified.[29]

Here we posit that a sequential catalysis strategy using CO as an intermediate species can be used to tune the C_2 product distribution in aqueous CO_2R. To realize such a strategy, a system consisting of 2 sites can be envisioned whereby one site converts CO_2 to CO, which then diffuses to a second site where it is further reduced to the desired product. More specially, to produce the intermediate, we will use a metal such as Ag or Au, which produces CO with high selectivity. If this metal is placed in close proximity to Cu, the CO can diffuse to the Cu where it can react further, along with the CO_2 which is being reduced concurrently.

Sequential or cascade catalysis has investigated previously in the CO_2 reduction literature. Sanford and co-workers used 3 homogeneous catalysts to thermally hydrogenate CO_2 selectively to methanol via formic acid and formate ester intermediates.[30] Jiang and co-workers used 3 enzymes co-located in micelles to convert CO_2 to methanol with NADHP as the reductant.[31] Very recently, Yang, Somorjai, and co-workers demonstrated sequential thermal CO_2 reduction using CeO_2-Pt/SiO_2-Co core-shell particles, with transport of the CO intermediate proceeding from the core to the shell via the mesoporous SiO_2.[32] Furthermore, recent calculations by Vesborg and Seger have shown that breaking down the multistep CO_2R process into two steps, first from CO_2 to CO on one catalyst and subsequently from CO to further reduced products such as ethanol on another catalyst, might be a strategy to overcome fundamental efficiency limitations.[33]

In EC CO_2R, there have been numerous recent studies including bimetallic alloys[34,35] and phase separated nanoparticles.[36–41] Of interest here are those for which a CO generating metal is used in tandem with Cu for which a sequential catalysis mechanism is proposed. Yeo and co-workers studied EC CO_2R on Zn-Cu composite nanoparticles and attributed increased ethanol selectivity to "spillover" of CO generated from Zn sites onto Cu sites, where it was further reduced.[42] Very recently, Meyer and co-workers found that a mixture of Ag and Cu nanoparticles was able to generate acetate with up to 21% selectivity and a mechanism involving CO transport from the Ag to the Cu was tentatively proposed.[43] Lee and co-workers investigated a Ag-incorporated Cu electrode and observed higher ethanol selectivity.[41] However, in this case, the selectivity to ethanol was attribute to biphasic Ag-Cu boundaries.

The requisite length scale required for sequential catalysis required merits discussion. The transport of the intermediate species between the different active sites competes with diffusion away from them. It is exactly this trade-off between inter-site transport and diffusion to the bulk which limits sequential catalysis in enzymatic systems to active site spacings of only a few nm.[44] Similarly, although there are some exceptions,[45] the surface transport required for "spill-over" effects in multi-site heterogeneous catalysis also limits length scales to the nm scale.[46,47] While we are not aware of an experimental measurement of CO surface diffusion under aqueous CO_2 conditions,[48–50] we will assume, based on measurements of surface diffusion rates of other adsorbed species,[51] that this process will also be constrained to the nanoscale.

Instead, we will show, both by simulations and experiment, that sequential catalysis can be affected *on the micron scale*, with diffusional transport of the intermediate CO in the liquid phase. This is possible due to the far higher density of catalytic sites (and corresponding molar fluxes) on the surface of a metal electrocatalyst, compared to, for example, enzymatic systems. Specifically, for a bifunctional system with a CO-producing metal (Ag or Au) and Cu, we will show that CO transport and further conversion is possible for spacing up to fractions of the diffusion layer thickness, which is typically on the order of ~100 µm in electrochemical systems.[52] We emphasize that long range transport of active species from one electrode to another is not unprecedented in electrochemistry and is the operating principle of a rotating ring disk electrode.[52–55] We also note that interdigitated electrodes relying on liquid phase diffusion of species from one electrode to another have been successfully employed for electroanalysis purposes.[56,57] However, in these cases, one electrode is used to reduce a species and the second is used to oxidize the intermediate.

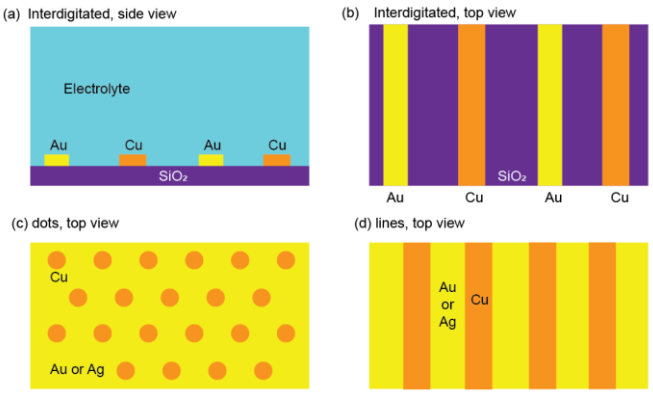

Figure 1. Schematics of interdigitated bimetallic electrodes, (a) and (b), and micropatterned electrodes, (c) and (d). Separation of the two metals in the interdigitated design will allow for their independent operation. In all three designs, the areal ratio of the CO-producing metal, Au or Ag, to Cu can be varied.

The sequential catalysis concept is realized in the two micropatterned systems shown in Fig. 1. The first consists interdigitated lines of Au and Cu on an insulating SiO_2 substrate (Fig. 1a). The Au lines are electronically isolated from the Cu lines, which allows for the independent actuation of just one set of lines or both at the same time, Figure 1b. The Au lines generate CO, while the Cu lines reduce the CO and also the externally supplied CO_2 to further reduced products. The ratio

of Au and Cu can be adjusted by varying the width of the Au lines, while keeping the width of Cu lines constant, allowing for a systematic study. Having a larger ratio of Au to Cu should result in higher CO availability per active Cu site present. Our approach, in which both sets of lines are used synergistically in two successive reduction steps is a new concept, which to the best of our knowledge does not have a precedent in the electrocatalysis literature. In the second system, Cu consisting of 2 different shapes and sizes are patterned onto a Ag or Au substrate (Figs. 1c and 1d); the exposed Ag or Au generates CO. We will show that these bimetallic microfabricated catalysts allow for considerable tuning of the CO_2R product distribution.

In these systems, we will show that majority of the CO generated from Au/Ag is able to diffuse towards Cu where it is further reduced as evidenced by significantly low CO partial current densities, even at large Au/Ag coverages. Lower areal coverages of Cu favor C_2/C_3 oxygenates, whereas higher areal coverages favor ethylene, allowing for tuning of the oxygenates to ethylene ratio from 0.59 to 2.39 (while maintaining C_2/C_3 product selectivity at >60% faradaic efficiency). Additionally, typically minor oxygenate products such as acetaldehyde and acetate produced on Cu is greatly enhanced, e.g, from 1% to >10%, on these systems as a result. Finally, we will also demonstrate that generating the CO locally in close proximity to the Cu produces a catalytic outcome that is different from simply using a gas feed mixture of CO_2/CO at ambient pressure. This is because a non-equilibrium state is established on the surface of the Cu, whereby a high local concentration of CO can exist, above the solubility limit, without reducing the bulk CO_2 concentration.

Results and Discussion

Simulations of intermediate species transport

To develop our design for our interdigitated AuCu device system, we simulated the transport of CO from Au lines to Cu lines as well as to the edge of the diffusion layer (see ESI for full modelling details). Four different devices were modelled, in which Au and Cu lines have the same spacings apart (26 µm) and same width of Cu lines (4.2 µm), but different widths of the Au lines (3.5, 16.25, 35.0 and 147.5 µm). Such an arrangement yields 4 different Cu compositions (by geometric area), which are 55%, 21%, 11% and 3% respectively. For a X% device, X% refers to the ratio of the geometric area of the Cu lines to the total metal area (total metal area = Cu area + Au area). Thus, the 55% AuCu device has the highest Cu coverage, but the lowest Au coverage. On the other hand, the 3% AuCu device has the lowest Cu coverage, but the highest Au coverage.

A CO molar flux of 1.6 x 10^{-8} mol cm^{-2} s^{-1} was fixed on the Au, which is equivalent to a partial current density of 3 mA cm^{-2} to CO. This value is within range of the expected production rate when a potential of ~-0.8 V to -1.2 V vs RHE is applied.[58] As the CO consumption rate on the Cu is not known *a priori*, a boundary condition of zero CO concentration was set on the surface of Cu (ideal sink, see ESI Fig. S2 for calculations which evaluate the effect of sink ideality). Figure 2 shows the CO concentration profile and the fraction of the CO generated on the Au which is further converted on the Cu for the 4 different relative areal coverages of Cu. The simulation clearly shows that a significant fraction of the CO generated on the Au is available for further reduction on the Cu and that the devices will allow for control of the flux.

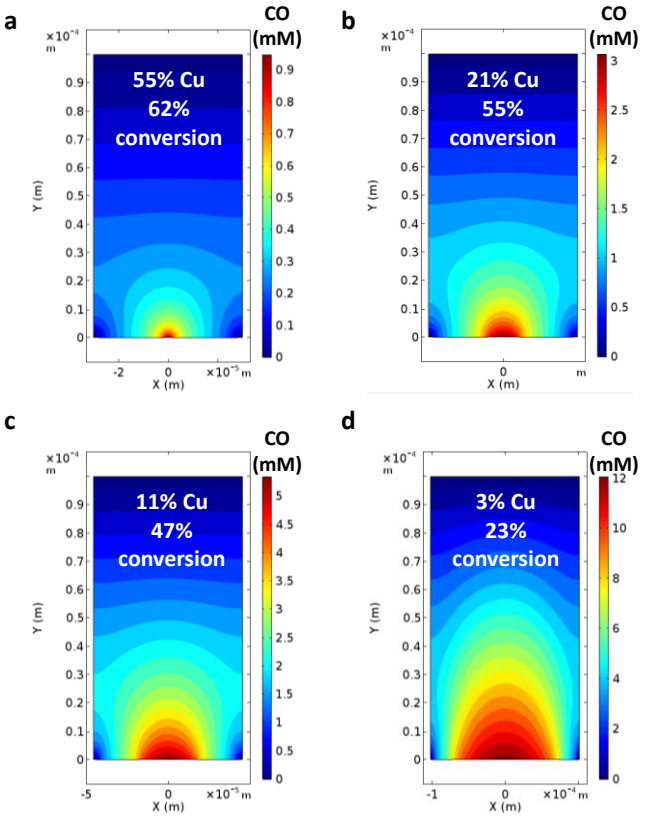

Figure 2. Calculated CO concentration contours in mM for interdigitated devices with relative area coverages of Cu ranging from 55% (a) to 3% (d). The CO-producing metal is placed in the centre of the unit cell and the Cu is placed at the corners (See Fig. S1 ESI for schematic of the modelling geometry). The width of the Cu lines is fixed at 4.2 µm while the Au line width is varied from 3.5 µm (a) to 147.5 µm (d). The spacing between the metal lines is fixed at 26 µm. A current density of 3 mA cm^{-2} for the formation of CO on the Au as assumed. The fraction of the CO produced on the Au which is further converted after diffusion to the Cu is indicated, assuming that Cu is an ideal sink for the CO.

The modeling results show that in some cases, the concentration of CO near the surface exceeds the solubility limit of 1 mM. Bubble formation, which could reduce the CO transfer and potentially block surface catalytic would be a potential concern. However, supersaturation of a gas on the surface of an electrode from which it is produced is a well-known effect.[59–63] Notably, smooth electrode surfaces of the type we will employ here have been shown to suppress bubble nucleation, allowing for a high degree of supersaturation.

Microfabricated bifunctional cathode with independent actuation

Four AuCu device systems were fabricated by photolithography with Cu and Au lines on an insulating SiO_2 substrate (see ESI for fabrication details). Figure 3a shows a schematic of the AuCu device, with the design parameters for the 4 different devices

in a table. Figures 3b and 3c show the SEM and EDX images for the 21% AuCu device. As the lines in this device are electronically isolated, either or both can be actuated via an external circuit with on/off switches (Fig. 3a).

Firstly, we show that the Au and Cu lines can be actuated independently. Unless otherwise stated, electrochemical evaluations were performed at -1.0 V vs RHE in CO_2 saturated 0.1 M $CsHCO_3$ electrolyte. Figure 4a shows the product distribution when only the Au lines are actuated. For all 4 devices, the CO faradaic efficiency is ~53%, with hydrogen making up majority of the rest of the products (~39%). A small fraction of hydrocarbons (~2%) was observed in all cases, which is attributed to small amounts of Cu contamination on the Au lines as a result of the deposition process. Figure 4b shows that when only the Cu lines are actuated at -1.0 V vs RHE the product distribution is qualitatively similar to that of the Cu foil reference with a faradaic efficiency to oxygenates of about 20%. Note that although formate is an oxygenate, we will not classify it as an oxygenate in our analysis because this product cannot be derived from CO.[64] Thus, for the entirety of the manuscript, we will refer to C_2/C_3 oxygenates solely as "oxygenates" and these include glyoxal, glycolaldehyde, acetate, ethylene glycol, acetaldehyde, ethanol, hydroxyacetone, allyl alcohol, propionaldehyde and propanol.

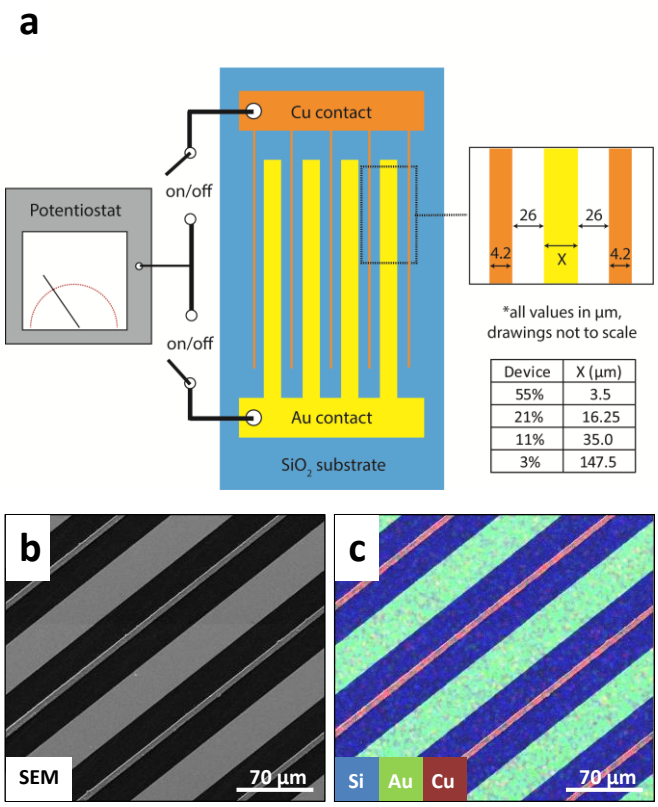

Figure 3. (a) Schematic of the interdigitated AuCu device, showing the design parameters for the 4 different devices in a table. Externally connected on/off switches linked to a potentiostat can be turned on and off to actuate both Au and Cu lines, Au only or Cu only. (b) SEM and (c) EDX images of the 11% AuCu device with Si in blue, Au in green and Cu in red. See Figures S4 to S9 for more information. Note: for a X% device, X% refers to the ratio of the geometric area of the Cu lines to the total metal area.

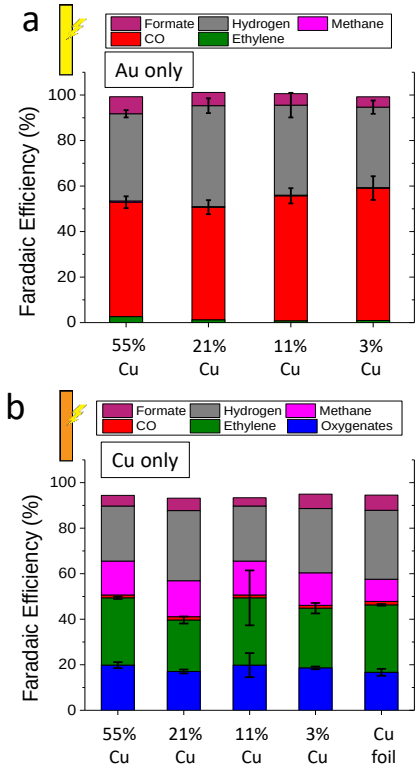

Figure 4. Faradaic efficiency plots for the 4 different AuCu devices when: (a) only Au lines are actuated and (b) when only Cu lines are actuated. In (b), Cu foil data is shown as a reference. For a X% device, X% refers to the ratio of the geometric area of the Cu lines to the total metal area. Errors bars are given for CO and H_2 in (a) and ethylene and oxygenates in (b). Error bars are standard deviations for replicate experiments, typically 3.

To study the effect of CO transport from the Au to the Cu, both the Au and Cu lines were actuated at the same time (Figs. 5a and 5b); there are 2 main effects. Firstly, the partial current density to CO (Figure 5c) drops significantly when both Au and Cu are actuated compared to when only Au is actuated, showing that CO formed on the Au is consumed by the Cu lines, validating the sequential catalysis concept. Secondly, analysis of the oxygenates to ethylene ratio (in terms of faradaic efficiency) shows a steady increase with decreasing Cu coverage, from a value of 0.67 for the 55% device to 1.18 for the 3% device (Figure 5d). Comparatively, when only Cu is actuated, the oxygenates to ethylene ratio for all devices is a lower value of ~0.71.

Energy & Environmental Science

ARTICLE

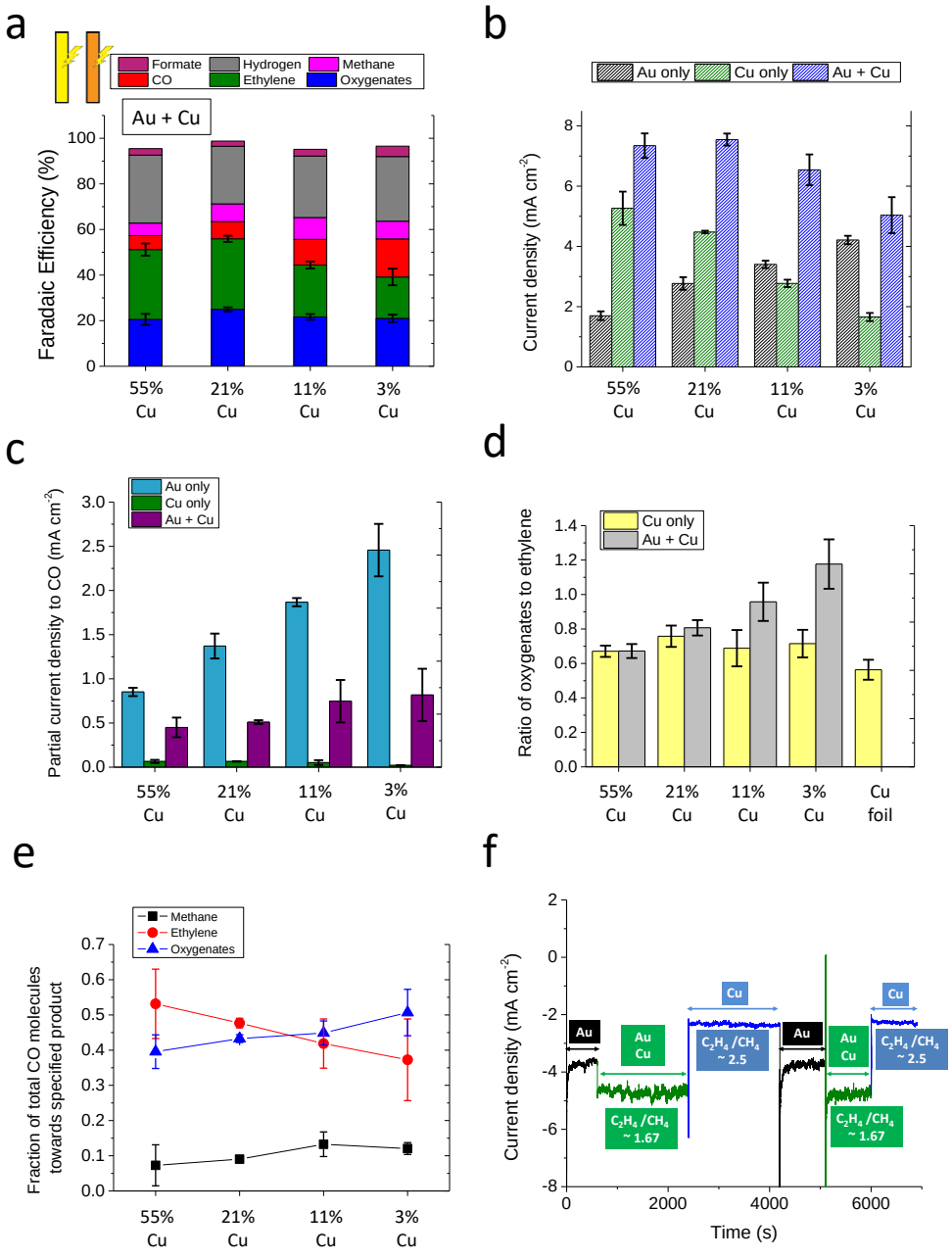

Figure 5. (a) Faradaic efficiency plots for the 4 different AuCu devices when both Au+Cu lines are actuated. Error bars are shown for oxygenates and ethylene. (b) Total current densities and (c) partial current densities to CO for the Au only, Cu only and Au+Cu case. (d) Ratio of oxygenates to ethylene (in terms of faradaic efficiency) for the 4 AuCu devices for both cases when only Cu is actuated and when both Au and Cu are actuated. (e) Fraction of total CO molecules going towards methane, ethylene or oxygenates (see Table S3 for detailed calculations). See Figure S10 and S11 for breakdown of the oxygenates for Au+Cu. (f) Current density profile when different sets of lines are actuated for the 3% AuCu device. Black: Au only, blue: Cu only and green: Au and Cu. When Au lines are actuated, an observable increase in the methane to ethylene ratio is observed, as would be expected from (e). Note: where appropriate, Cu foil data is shown as a reference. Also, for a X% device, X% refers to the ratio of the geometric area of the Cu lines to the total metal area. Error bars are standard deviations for replicate experiments, typically 3.

Energy & Environmental Science

ARTICLE

In CO_2R, it is known that CO is the central intermediate from which ethylene, oxygenates and methane are derived[18]. The CO consumption rate required for generating each product can be calculated from their respective partial current densities and, from this, the fraction of CO molecules going towards various products can be obtained (see Table S3 in ESI for detailed calculations and discussion). Representing the product distribution in such a way (as compared to the FE scale) accounts for the fact that different products require different numbers of electron transfers to generate one mole of product (e.g. 12 mol e^- and 8 mol e^- per mol of ethanol and acetate respectively). Figure 5e shows that lower Cu areal coverage (higher predicted local CO concentration cf. Fig. 2) increases the fraction of CO going towards oxygenates, while the fraction to ethylene decreases, with the methane fraction staying relatively constant. Analysis of the difference in partial current densities for methane, ethylene and oxygenates for the case when Cu only versus when both Au and Cu are actuated (Figure S12) reveals that CO transfer results in an increase in the partial current density towards both ethylene and oxygenates. However, at the lower Cu ratios, the increase in partial current density towards oxygenates is larger than that for ethylene, leading to a higher oxygenate to ethylene ratio.

Figure 5e shows that with decreasing areal coverage of Cu, the ethylene fraction of the products decreases while the methane fraction remains constant with CO transfer. This means that the methane to ethylene ratio (in terms of faradaic efficiency) should become higher when the sequential pathway is activated by turned on the Au lines. This is indeed the case, as shown in Fig. 5f; the ethylene to methane ratio does indeed become lower when the Au lines are turned on (in this experiment only the gas phase products could be quantified as a function of time). Also, the reproducibly of both the current density and the gas phase product distribution clearly show the independent control of the two catalytic metals and rule out any possible effects from alloying or cross contamination.

Microfabricated bifunctional electrode with reduced spacing

We hypothesized the sequential catalysis pathway could be further enhanced by patterning Cu directly onto a Au substrate. This geometry enables the Cu and the CO source to be placed closer to each other (limitations of photolithography prevented us from fabricated interdigitated devices with closer spacings). Cu lines of 8.6 µm width spaced 39 µm apart were fabricated onto a Au substrate (see ESI for fabrication details) producing a surface with 18.2% areal coverage of Cu (Figure S16, ESI). These catalysts yield an oxygenate to ethylene ratio of 1.23 (Figure S20, ESI). Although this oxygenate to ethylene ratio is relatively high, the catalyst has a relatively high faradaic efficiency of 36.4% to hydrogen. This is most likely due to the Au substrate itself exhibiting a high hydrogen faradaic efficiency (44.4%) at this potential (Figure S20, ESI).

We therefore turned to a different metal to produce CO at -1 V vs RHE, while producing less hydrogen. Ag and Zn are two possibilities; here we used Ag due to its higher CO partial current density and CO faradaic efficiency.[15,58] Cu lines of fixed 8.6 µm width and varying spacings (2.5 – 39 µm) were fabricated onto a Ag substrate (Figure 6a and Figure S17, ESI), which yields catalysts with 18.2- 77.2% areal coveragse of Cu. A control sample was fabricated as well, in which 100% of the Ag surface was coated with Cu (Figure S15c, ESI). Figures 6b and 6c reveal a trend similar to that of the AuCu devices; a lower areal coverage of Cu results in higher oxygenate to ethylene ratios. Going from 77.2% Cu to 18.2% Cu, this ratio increases from 0.72 to 1.15 and the faradaic efficiency to oxygenates can be tuned from 21.3% to 28.8%. For the control case where 100% of the Ag substrate is covered by Cu (100% Cu), the oxygenates to ethylene ratio (0.59) is very similar to that of Cu foil reference (0.56), as expected. Also, as the Cu areal coverage decreases, the faradaic efficiency to hydrogen goes down as well, with a value of only 16.0% for 18.2% Cu. This compares favorably against the case where a Au substrate was used instead, which had a faradaic efficiency of 36.4% to hydrogen. Also, the faradaic efficiency to CO is observed to go up with lower Cu coverage, indirectly indicating a larger molar flux of CO available to Cu.

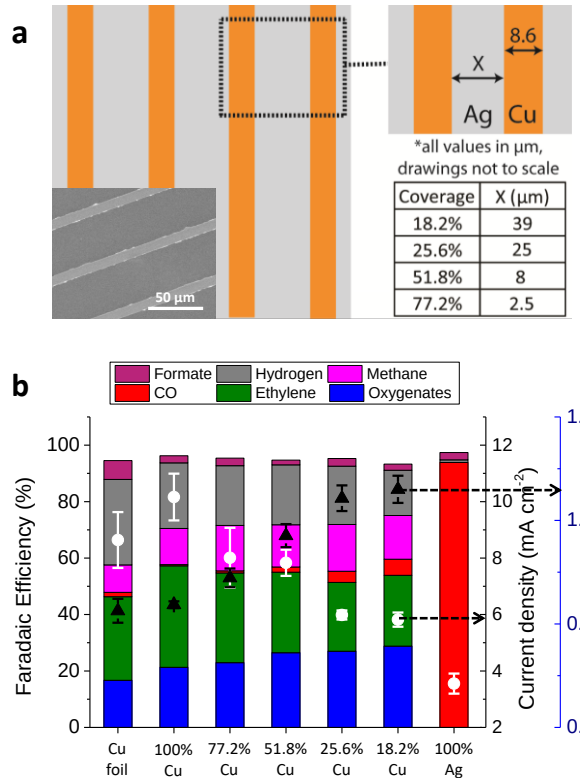

Coverage	X (µm)
18.2%	39
25.6%	25
51.8%	8
77.2%	2.5

Figure 6. (a) Schematic of the Cu lines on Ag substrate system, with design parameters shown in a table. Inset shows a SEM image of 18.2% Cu lines on Ag. (b) Faradaic efficiency for Cu lines on Ag system as a function of Cu areal coverage. 100% Ag refers to the Ag substrate. Current density (black triangles) and ratio of oxygenates to ethylene (white dots) as a function of Cu areal coverage. Error bars are standard deviations for replicate experiments, typically 3. More SEM images (Figure S18) are available in the supporting information. Error bars for oxygenates and ethylene are given.

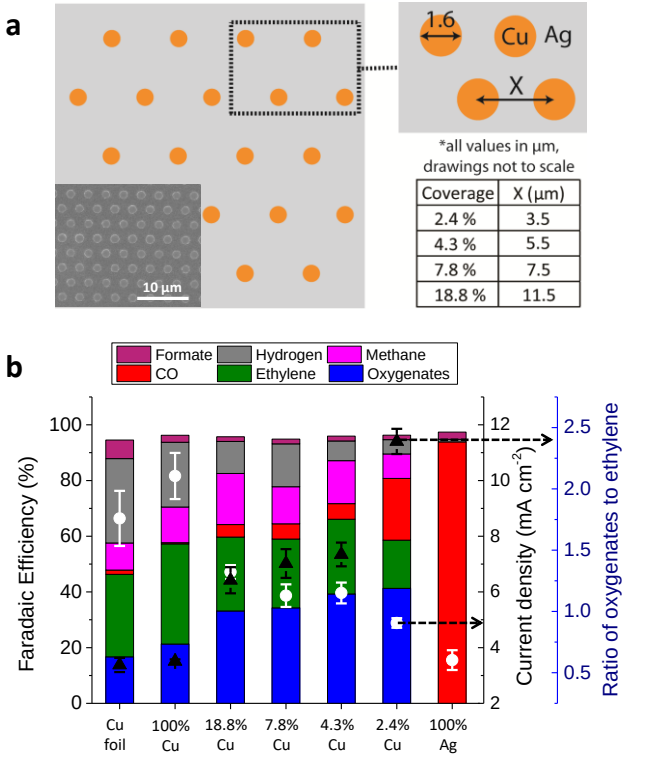

Coverage	X (µm)
2.4 %	3.5
4.3 %	5.5
7.8 %	7.5
18.8 %	11.5

Figure 7. (a) Schematic of the Cu dots on Ag substrate system, with design parameters shown in a table. (b) SEM image of 18.8% Cu dots on Ag. Faradaic efficiency towards various products for Cu dots on Ag system as a function of Cu areal coverage. 100% Ag refers to the Ag substrate. Current density (black triangles) and ratio of oxygenates to ethylene (white dots) as a function of Cu areal coverage. Error bars are standard deviations for replicate experiments, typically 3. More SEM images (Figure S22) are available in the supporting information. Error bars for oxygenates and ethylene are given.

To further increase the oxygenate to ethylene ratio in the Cu on Ag system, we hypothesized that CO transfer could be made more facile by shrinking the dimensions of the Cu. Furthermore, the trends observed in Fig. 6b suggest that further improvements could be made by going to even lower areal coverages of Cu. To this end, 1.6 µm Cu dots were fabricated in a hexagonal pattern with 4 different nearest neighbor distances (see Figure 7a and Figure S18) to achieve 4 different Cu areal coverages (2.4, 4.3, 7.8 and 18.8%). As expected, even higher oxygenate to ethylene ratios were obtained (Figure 7b), with samples possessing a lower Cu areal coverage having a higher ratio. With this system, the ratio of oxygenates to ethylene can be tuned from 1.25 with 18.8% Cu all the way to 2.39 with 2.4% Cu and the faradaic efficiency to oxygenates rising to 41.3%. Interestingly for the 2.4% Cu case, the faradaic efficiency for oxygenates (41.3%) is even higher than that for methane and ethylene combined (26.1%). Furthermore, the faradaic efficiency to hydrogen for this catalyst was only 5.14%, although faradaic efficiency to CO was at 22.2%, indicating that diffusional escape of the CO at this low Cu coverage. In general, it is observed that lower Cu coverages result in lower faradaic efficiencies to hydrogen and is likely due to Ag substrate producing minimal amounts of hydrogen at this potential (Figure 7b).

Figure 8a shows the fraction of total CO molecules going to methane, ethylene and oxygenates for the Cu dots/lines system (analysis similar to that used for Figure 5e, with calculation details in Table S3). This figure highlights the considerable tunability of the sequential catalyst system; the fraction of CO molecules going to oxygenates can be varied from 0.33 to 0.67 and the fraction to ethylene from 0.53 to 0.24. The fraction towards methane appears relatively constant, however slight decreases are observed at lower Cu coverages. In Figure 8b, the breakdown of the oxygenates into its various components for the Cu dots/lines catalyst systems is plotted (for further breakdown of the oxygenates see Figure S21 and S22, ESI). Interestingly, the oxygenates with the largest increases in faradaic efficiency at lower Cu coverages are acetaldehyde and acetate. The 2.4% Cu dots system exhibits a faradaic efficiency of 14.4% to acetaldehyde and 6.8% to acetate. Comparatively, on Cu foil and 100% Cu, these 2 products are only generated in minor amounts (~0.6% for acetaldehyde and ~0.7% for acetate). On the other hand, the faradaic efficiency towards ethanol and propanol remain relatively constant with Cu coverage. The inset to Fig. 8b shows that the total C_2/C_3 faradaic efficiency for all sequential catalyst systems; this value is maintained in the 50-65% range regardless of Cu coverage.

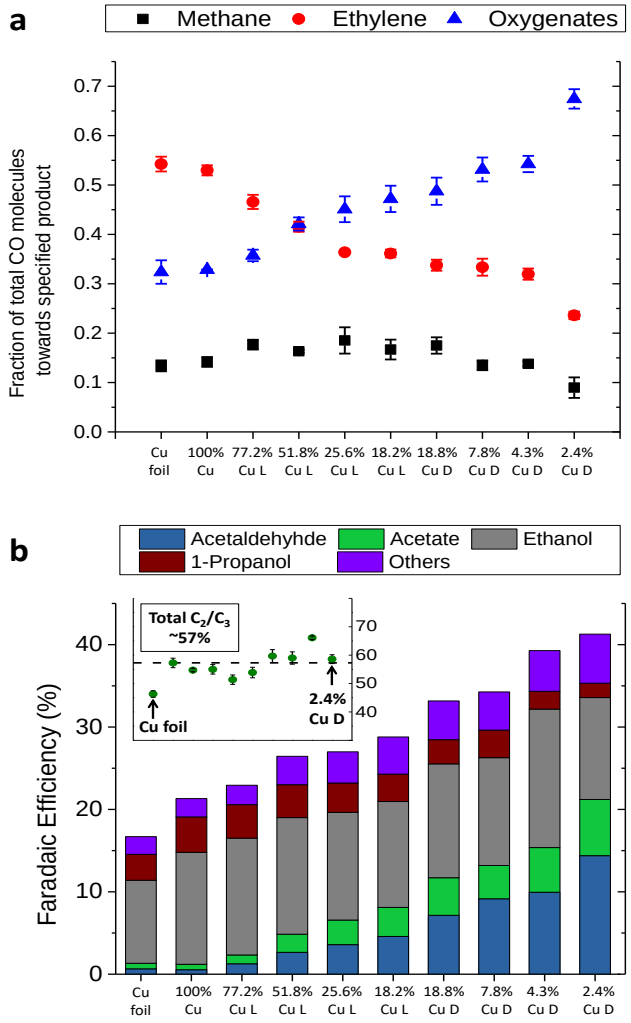

Figure 8. (a) Fraction of total CO molecules going towards methane (black), ethylene (red) and oxygenates (blue). (b) Breakdown of the oxygenates into its various components for the Cu dots/lines on Ag substrate. Further breakdown of the components is available in Figure S21 and S22, ESI. The inset shows the total C_2/C_3 faradaic efficiency for all catalysts in the Cu dots and lines system. D refers to dots and L refers to lines.

Control experiments

In contrast to the interdigitated AuCu devices, the microfabricated systems have an exposed Cu/Ag interface. Therefore, control experiments were performed to eliminate the possibility of the Cu/Ag interface having a significant catalytic effect. A sample was made with a 30 nm carbon interlayer introduced via sputter deposition in between the Ag substrate and the Cu dots (see Figure S19, ESI). With the carbon interlayer there are no Cu/Ag interfaces present. When tested at -1.0 V vs RHE, a high oxygenate to ethylene ratio of 2.25 was observed (Figure S23), similar to the case without the carbon layer. Also, we note that regardless of whether a Au or Ag substrate was used, 18.2% lines of Cu areal coverage resulted in similar oxygenate to ethylene ratios of 1.15 and 1.23 for Ag and Au respectively (see Figure 6b and Figure S20, ESI), even though they have different metal-metal interfaces. Also, the partial current densities to ethylene and oxygenates were calculated for both cases and these values were very similar as well (Figure S24). We conclude that interface sites do not have a significant role in our micropatterned bimetallic catalysts.

To rule out the possibility Ag has a catalytic role other than making CO, CO reduction was carried out at -1.0 V vs RHE in 0.1 M phosphate buffer (pH 7) and at -0.7 V vs RHE in both the 0.1 M CsOH and 0.1 M $CsHCO_3$ electrolyte for both 100% Cu on Ag and 18.8% Cu dots on Ag. The observed oxygenate to ethylene ratios for both catalyst samples and for both potentials and electrolyte conditions were similar (Figure S25).

Reduction experiments on a Cu electrode were carried out with a gas mixture feeds of CO_2/CO (90/10, 80/20/ 70/30) to investigate if having a background concentration of CO could produce effects similar to those found for the micropatterned catalyst systems. However, using a partial CO feed results in the lowering of the aqueous CO_2 concentration, resulting in conditions where selectivity to hydrogen is increased (Table S9). Moreover, there is no observable change in the ethylene to oxygenates ratio (Tables S9 and S10). We therefore conclude that the catalytic outcomes we obtained on the micropatterned catalyst systems cannot be obtained by simply flowing in mixtures of CO_2 and CO. This is because in our system, a local source of CO can be provided to the Cu regions without reducing the bulk CO_2 concentration, thereby establishing a non-equilibrium state on the surface (see Tables S11 to S12).

Finally, it has been demonstrated that pH can have an effect on the CO_2R product distribution.[65,66] To determine if pH changes could influence catalytic outcomes in this work, the surface pH was calculated using a 2D computational model (Figure S26 and Tables S5-S8). Modeling results reveal that for the interdigitated AuCu devices, the surface pH at the 2 metals is ~10 and actual pH values differ by not more than 0.7 pH units. For the Cu dots/lines on Ag system, the surface pH is also ~10 and actual pH values differ by not more than 0.5 pH units. We note that larger changes in pH are required to cause significant changes in the product distribution,[66] and we thus conclude that pH changes alone cannot account for the experimental observations.

Mechanism of selectivity to oxygenates via sequential catalysis

Finally, we consider the mechanism causing increased oxygenate production from CO transfer. It is plausible that CO transfer could induce a higher *CO coverage over Cu during CO_2R. Theoretical calculations have suggested that the main surface species on Cu surface sites are *CO and *H, with the coverage of each intermediate depending on the surface facet, strain, applied potential and partial pressure of CO.[28,29,67,68] According to Norskov and co-workers,[68] the *CO and H* coverages determine the CO dimerization rate and surface hydrogenation rate respectively. When a local source of CO is present, the chemical potential of CO on Cu can be raised, leading to a higher *CO coverage and a lower *H coverage.[68] A higher *CO coverage can result in a decrease in *CO binding energy,[68,69] which would shift Cu to the left along the theoretical activity volcano for CO_2R[70] and therefore induce a change in the catalytic properties of Cu. Furthermore, a lower *H coverage might result in a slower surface hydrogenation rate of CO

dimers. A high *H coverage could be required to sustain hydrogenation of CO dimers all the way to ethylene, with a low *H coverage possibly favoring the formation of oxygenates instead. This could also be the reason why large amounts of acetaldehyde are observed as further hydrogenation to form ethanol could be inhibited. Acetaldehyde disproportionation then results in ethanol and acetate formation as shown by Koper and co-workers.[71]

An increase in oxygenates at the expense of ethylene is also evident in the experimental work of Kanan and co-workers, in which CO reduction at partial pressures of 2.4 atm and 1.0 atm was carried out on "oxide-derived" Cu catalyst over a range of potentials.[19] At the higher CO partial pressure, a higher *CO coverage is likely to have been induced, leading to a decrease in FE and partial current density for ethylene and an increase for oxygenates (Figure S27) which was observed across all the potentials that were tested.

Energy efficiency considerations

For CO_2R to become a practical technology, it is important that the conversion reactions have high energy efficiency, defined as the total free energy gain of producing the products divided by the electrical energy provided to the electrochemical system. Using an analysis similar to that of our previous work,[72] we estimated the energy efficiencies of our patterned Cu dots/lines catalysts if operated in an optimized system. We find that energy efficiencies towards C_2/C_3 products are the highest for the case with 4.3% Cu dots (21.4%) and that 100% Cu (14.3%) and Cu foil (12.5%) have lower efficiencies; see SI Tables S13 and S14 for calculation details and full analysis. The higher energy efficiency of the catalyst with lower areal coverage of Cu is due to the combined effect of maintaining a high C_{2+} FE (see inset Figure 8b), whilst suppressing hydrogen evolution. A low partial current to hydrogen formation is important as it reduces the overall cell voltage at a given C_{2+} product production rate. This effect results from a reduction in IR losses from the membrane and solution resistances as well as reduced overpotential requirements at the anode. Considering total energy efficiencies towards all CO_2R products, again lower areal coverages of Cu yielded higher efficiencies. For example, 2.4% Cu dots (32.8%) have a higher efficiency compared to 100% Cu (18.1%) or Cu foil (17.5%). Additionally, the electrical energy consumed per mole of C_2/C_3 product generated was calculated as well (Table S15). Similarly, systems with lower Cu coverage are observed to require less energy to generate C_2/C_3 products. However, this does come at the cost of a lower partial current density towards these products.

Conclusions

In summary, we have shown that CO generated by a nearby CO producing catalyst can transfer onto Cu resulting in increased oxygenate production. This is demonstrated with Cu dots or lines of fixed dimensions patterned directly onto a Ag substrate and in such a system, we are able to systematically tune the product distribution of Cu and adjust the ratio of oxygenates to ethylene from 0.59 to 2.39. We postulate that this effect could be due to an increase in *CO coverage on Cu.

Conflicts of interest

There are no conflicts to declare.

Acknowledgements

This material is based upon work performed by the Joint Center for Artificial Photosynthesis, a DOE Energy Innovation Hub, supported through the Office of Science of the U.S. Department of Energy under Award Number DE-SC0004993. Photolithography was performed using facilities in the Electronic Materials Program, which is supported by the Director, Office of Science, Office of Basic Energy Sciences, Materials Sciences and Engineering Division of the U.S. Department of Energy, under contract no. DE-AC02-05CH11231. We thank the Molecular Graphics and Computation Facility, College of Chemistry, University of California Berkeley, supported by National Science Foundation grant CHE-080405, for providing access to computing resources Y.L. acknowledges the support of an A*STAR National Science Scholarship. The authors thank Fiona M. Doyle and Kevin Chen for helpful discussions.

References

1 C. Graves, S. D. Ebbesen, M. Mogensen and K. S. Lackner, *Renew. Sustain. Energy Rev.*, 2011, **15**, 1–23.
2 A. Goeppert, M. Czaun, J.-P. Jones, G. K. Surya Prakash and G. A. Olah, *Chem. Soc. Rev.*, 2014, **43**, 7995–8048.
3 D. Kim, K. K. Sakimoto, D. Hong and P. Yang, *Angew. Chemie Int. Ed.*, 2015, **54**, 3259–3266.
4 S. Chu, Y. Cui and N. Liu, *Nat. Mater.*, 2016, **16**, 16–22.
5 J. H. Montoya, L. C. Seitz, P. Chakthranont, A. Vojvodic, T. F. Jaramillo and J. K. Nørskov, *Nat. Mater.*, 2016, **16**, 70–81.
6 J. Qiao, Y. Liu, F. Hong and J. Zhang, *Chem. Soc. Rev.*, 2014, **43**, 631–675.
7 Q. Lu, J. Rosen and F. Jiao, *ChemCatChem*, 2015, **7**, 38–47.
8 H. Mistry, A. S. Varela, S. Kühl, P. Strasser and B. R. Cuenya, *Nat. Rev. Mater.*, 2016, **1**, 16009.
9 B. Kumar, J. P. Brian, V. Atla, S. Kumari, K. A. Bertram, R. T. White and J. M. Spurgeon, *Catal. Today*, 2016, **270**, 19–30.
10 D. D. Zhu, J. L. Liu and S. Z. Qiao, *Adv. Mater.*, 2016, **28**, 3423–3452.
11 K. D. Yang, C. W. Lee, K. Jin, S. W. Im and K. T. Nam, *J. Phys. Chem. Lett.*, 2017, **8**, 538–545.
12 B. Khezri, A. C. Fisher and M. Pumera, *J. Mater. Chem. A*, 2017, **5**, 8230–8246.
13 G. O. Larrazábal, A. J. Martín and J. Pérez-Ramírez, *J. Phys. Chem. Lett.*, 2017, **8**, 3933–3944.
14 K. P. Kuhl, E. R. Cave, D. N. Abram and T. F. Jaramillo, *Energy Environ. Sci.*, 2012, **5**, 7050.
15 Y. Hori, in *Modern Aspects of Electrochemistry*, eds. C. G. Vayenas, R. E. White and M. E. Gamboa-Aldeco, Springer

New York, New York, NY, 2008, pp. 89–189.
16 M. Gattrell, N. Gupta and A. Co, *J. Electroanal. Chem.*, 2006, **594**, 1–19.
17 M. R. Singh, E. L. Clark and A. T. Bell, *Proc. Natl. Acad. Sci.*, 2015, **112**, E6111–E6118.
18 Y. Hori, R. Takahashi, Y. Yoshinami and A. Murata, *J. Phys. Chem. B*, 1997, **101**, 7075–7081.
19 C. W. Li, J. Ciston and M. W. Kanan, *Nature*, 2014, **508**, 504–507.
20 N. Gupta, M. Gattrell and B. MacDougall, *J. Appl. Electrochem.*, 2006, **36**, 161–172.
21 H. Zhong, K. Fujii, Y. Nakano and F. Jin, *J. Phys. Chem. C*, 2015, **119**, 55–61.
22 A. A. Peterson, F. Abild-Pedersen, F. Studt, J. Rossmeisl, J. K. Nørskov and J. K. Norskov, *Energy Environ. Sci.*, 2010, **3**, 1311–1315.
23 X. Nie, M. R. Esopi, M. J. Janik and A. Asthagiri, *Angew. Chemie Int. Ed.*, 2013, **52**, 2459–2462.
24 F. Calle-Vallejo and M. T. M. Koper, *Angew. Chemie Int. Ed.*, 2013, **52**, 7282–7285.
25 T. Cheng, H. Xiao and W. A. Goddard, *J. Phys. Chem. Lett.*, 2015, **6**, 4767–4773.
26 H. Xiao, T. Cheng, W. A. Goddard and R. Sundararaman, *J. Am. Chem. Soc.*, 2016, **138**, 483–486.
27 H. Xiao, T. Cheng and W. A. Goddard, *J. Am. Chem. Soc.*, 2017, **139**, 130–136.
28 W. Luo, X. Nie, M. J. Janik and A. Asthagiri, *ACS Catal.*, 2016, **6**, 219–229.
29 T. Cheng, H. Xiao and W. A. Goddard, *Proc. Natl. Acad. Sci.*, 2017, **114**, 1795–1800.
30 C. A. Huff and M. S. Sanford, *J. Am. Chem. Soc.*, 2011, **133**, 18122–18125.
31 X. Wang, Z. Li, J. Shi, H. Wu, Z. Jiang, W. Zhang, X. Song and Q. Ai, *ACS Catal.*, 2014, **4**, 962–972.
32 C. Xie, C. Chen, Y. Yu, J. Su, Y. Li, G. A. Somorjai and P. Yang, *Nano Lett.*, 2017, **17**, 3798–3802.
33 P. C. K. Vesborg and B. Seger, *Chem. Mater.*, 2016, **28**, 8844–8850.
34 S. Rasul, D. H. Anjum, A. Jedidi, Y. Minenkov, L. Cavallo and K. Takanabe, *Angew. Chemie Int. Ed.*, 2015, **54**, 2146–2150.
35 E. L. Clark, C. Hahn, T. F. Jaramillo and A. T. Bell, *J. Am. Chem. Soc.*, 2017, **139**, 15848–15857.
36 S. Ma, M. Sadakiyo, M. Heima, R. Luo, R. T. Haasch, J. I. Gold, M. Yamauchi and P. J. A. Kenis, *J. Am. Chem. Soc.*, 2017, **139**, 47–50.
37 Z. Chang, S.-J. Huo, W. Zhang, J. Fang and H. Wang, *J. Phys. Chem. C*, 2017, **121**, 11368–11379.
38 D. Kim, J. Resasco, Y. Yu, A. M. Asiri and P. Yang, *Nat. Commun.*, 2014, **5**, 4948.
39 S. Sarfraz, A. T. Garcia-Esparza, A. Jedidi, L. Cavallo and K. Takanabe, *ACS Catal.*, 2016, **6**, 2842–2851.
40 W. Luc, C. Collins, S. Wang, H. Xin, K. He, Y. Kang and F. Jiao, *J. Am. Chem. Soc.*, 2017, **139**, 1885–1893.
41 S. Lee, G. Park and J. Lee, *ACS Catal.*, 2017, **7**, 8594–8604.
42 D. Ren, B. S.-H. Ang and B. S. Yeo, *ACS Catal.*, 2016, **6**, 8239–8247.
43 Y. Wang, D. Wang, C. J. Dares, S. L. Marquard, M. V. Sheridan and T. J. Meyer, *Proc. Natl. Acad. Sci.*, 2018, **115**, 278–283.
44 I. Wheeldon, S. D. Minteer, S. Banta, S. C. Barton, P. Atanassov and M. Sigman, *Nat. Chem.*, 2016, **8**, 299–309.
45 D. V. V Esposito, I. Levin, T. P. P. Moffat and A. A. A. Talin, *Nat. Mater.*, 2013, **12**, 562–568.
46 J. Grunes, J. Zhu, E. A. Anderson and G. A. Somorjai, *J. Phys. Chem. B*, 2002, **106**, 11463–11468.
47 B. Wickman, Y. E. Seidel, Z. Jusys, B. Kasemo and R. J. Behm, *ACS Nano*, 2011, **5**, 2547–2558.
48 M. T. M. Koper, J. J. Lukkien, A. P. J. Jansen and R. A. van Santen, *J. Phys. Chem. B*, 1999, **103**, 5522–5529.
49 M. T. M. Koper, A. P. J. Jansen, R. A. van Santen, J. J. Lukkien and P. A. J. Hilbers, *J. Chem. Phys.*, 1998, **109**, 6051–6062.
50 C. Korzeniewski and D. Kardash, *J. Phys. Chem. B*, 2001, **105**, 8663–8671.
51 P. Ionita, A. Volkov, G. Jeschke and V. Chechik, *Anal. Chem.*, 2008, **80**, 95–106.
52 A. J. Bard and L. R. Faulkner, *Electrochemical Methods: Fundamentals and Applications*, John Wiley, New York, 2nd edn., 2001.
53 R. K. Das, Y. Wang, S. V Vasilyeva, E. Donoghue, I. Pucher, G. Kamenov, H.-P. Cheng and A. G. Rinzler, *ACS Nano*, 2014, **8**, 8447–8456.
54 J. Herranz, A. Garsuch and H. A. Gasteiger, *J. Phys. Chem. C*, 2012, **116**, 19084–19094.
55 S. Sankarasubramanian, J. Seo, F. Mizuno, N. Singh and J. Prakash, *J. Electrochem. Soc.*, 2016, **163**, A2377–A2384.
56 O. Niwa, *Electroanalysis*, 1995, **7**, 606–613.
57 H. Ojima, M. Umeda, M. Mohamedi and I. Uchida, *Electroanalysis*, 2003, **15**, 1677–1681.
58 K. P. Kuhl, T. Hatsukade, E. R. Cave, D. N. Abram, J. Kibsgaard and T. F. Jaramillo, *J. Am. Chem. Soc.*, 2014, **136**, 14107–14113.
59 G. Sakuma, Y. Fukunaka and H. Matsushima, *Int. J. Hydrogen Energy*, 2014, **39**, 7638–7645.
60 S. Jones, *Adv. Colloid Interface Sci.*, 1999, **80**, 27–50.
61 D. Fernández, P. Maurer, M. Martine, J. M. D. Coey and M. E. Möbius, *Langmuir*, 2014, **30**, 13065–13074.
62 T. Kadyk, D. Bruce and M. Eikerling, *Sci. Rep.*, 2016, **6**, 38780.
63 C. Brussieux, P. Viers, H. Roustan and M. Rakib, *Electrochim. Acta*, 2011, **56**, 7194–7201.
64 R. Kortlever, J. Shen, K. J. P. Schouten, F. Calle-Vallejo and M. T. M. Koper, *J. Phys. Chem. Lett.*, 2015, **6**, 4073–4082.
65 M. Ma, K. Djanashvili and W. A. Smith, *Angew. Chemie Int. Ed.*, 2016, **55**, 6680–6684.
66 K. J. P. Schouten, E. Pérez Gallent and M. T. M. Koper, *J. Electroanal. Chem.*, 2014, **716**, 53–57.
67 S. A. Akhade, W. Luo, X. Nie, N. J. Bernstein, A. Asthagiri and M. J. Janik, *Phys. Chem. Chem. Phys.*, 2014, **16**, 20429–20435.
68 R. B. Sandberg, J. H. Montoya, K. Chan and J. K. Nørskov, *Surf. Sci.*, 2016, **654**, 56–62.
69 Y. Huang, A. D. Handoko, P. Hirunsit and B. S. Yeo, *ACS Catal.*, 2017, **7**, 1749–1756.

70 C. Shi, H. A. Hansen, A. C. Lausche and J. K. Nørskov, *Phys. Chem. Chem. Phys.*, 2014, **16**, 4720.
71 Y. Y. Birdja and M. T. M. Koper, *J. Am. Chem. Soc.*, 2017, **139**, 2030–2034.
72 Gurudayal, J. Bullock, D. F. Srankó, C. M. Towle, Y. Lum, M. Hettick, M. C. Scott, A. Javey and J. Ager, *Energy Environ. Sci.*, 2017, **10**, 2222–2230.